

Boundary Constraint-free Biomechanical Model-Based Surface Matching for Intraoperative Liver Deformation Correction

Zixin Yang*, Richard Simon*, Kelly Merrell, Cristian. A. Linte.

Abstract—In image-guided liver surgery, 3D-3D non-rigid registration methods play a crucial role in estimating the mapping between the preoperative model and the intraoperative surface represented as point clouds, addressing the challenge of tissue deformation. Typically, these methods incorporate a biomechanical model, represented as a finite element model (FEM), used to regularize a surface matching term. This paper introduces a novel 3D-3D non-rigid registration method. In contrast to the preceding techniques, our method uniquely incorporates the FEM within the surface matching term itself, ensuring that the estimated deformation maintains geometric consistency throughout the registration process. Additionally, we eliminate the need to determine zero-boundary conditions and applied force locations in the FEM. We achieve this by integrating soft springs into the stiffness matrix and allowing forces to be distributed across the entire liver surface. To further improve robustness, we introduce a regularization technique focused on the gradient of the force magnitudes. This regularization imposes spatial smoothness and helps prevent the overfitting of irregular noise in intraoperative data. Optimization is achieved through an accelerated proximal gradient algorithm, further enhanced by our proposed method for determining the optimal step size. Our method is evaluated and compared to both a learning-based method and a traditional method that features FEM regularization using data collected on our custom-developed phantom, as well as two publicly available datasets. Our method consistently outperforms or is comparable to the baseline techniques. Both the code and dataset will be made publicly available.

Index Terms—Non-rigid liver registration, Biomechanical model, Deformation correction, Image-guided surgery.

I. INTRODUCTION

IN image-guided liver surgery (IGLS), preoperative imaging modalities such as Computed Tomography (CT) or Magnetic Resonance Imaging (MRI) provide detailed insights into the liver’s internal structure, revealing information about tumors and vessels. However, these modalities are not commonly utilized intraoperatively due to practical constraints. Instead, alternative imaging techniques are employed during surgery, including tracked ultrasound [1], [2], cone-beam CT (CBCT) [3], and optical methods [4]–[8].

This work was supported by the National Institute of General Medical Sciences of the National Institutes of Health under Award No. R35GM128877 and by the Office of Advanced Cyber-infrastructure of the National Science Foundation under Award No.1808530. (Corresponding author: Zixin Yang.)

Zixin Yang, Richard Simon, Kelly Merrell, and Cristian. A. Linte are with the Center for Imaging Science and Department of Biomedical Engineering, Rochester Institute of Technology, Rochester, NY 14623 USA. (Email:yy8898, rasbme, kam1217, calbme@rit.edu)

Zixin Yang and Richard Simon contributed equally.

To integrate subsurface information from preoperative CT/MRI into the surgeon’s intraoperative view, registration methods are employed to map critical information from the preoperative images into the intraoperative scene. Rigid registration is often used to align data collected in different coordinates. However, the initial configuration of the liver at the start of the intervention can significantly deviate from its preoperative state. Studies indicate that the deformation of the anterior surface of the liver can exceed 10 mm during laparoscopic liver surgery (LLS) and 7 mm during open liver surgery (OLS) [9]. In clinical contexts, the target registration error is expected to be below 5 mm [4]. Therefore, non-rigid registration becomes essential to correct for such deformations.

Registration methods are broadly categorized into intensity-based [10] and geometric-based [11]–[13] approaches based on the type of information utilized to establish correspondences between the pre-and intraoperative data. Intensity-based methods employ pixel or voxel intensities for aligning images. However, challenges arise from intensity variations across different imaging modalities, such as CT to ultrasound, impacting the efficacy of these methods.

Geometric-based registration methods can be further classified based on the availability of 3D information extracted from intraoperative imaging. For scenarios where only 2D information is available, as with intraoperative monocular laparoscopes, 3D-2D registration methods are typically employed [11], [12]. In contrast, when intraoperative imaging modalities provide 3D information, usually presented as point clouds, 3D-3D registration methods [1], [5], [6] are preferred, as including 3D information introduces additional constraints to enhance registration accuracy [13].

This study focuses on the 3D-3D non-rigid registration problem in IGLS. Unlike the typical 3D-3D non-rigid registration problem in the computer vision [14], where the primary focus is achieving surface matching accuracy, the problem in IGLS emphasizes the necessity for the estimated organ deformation to be realistic, with a crucial consideration for the deformation beneath the tissue surface. Biomechanical models, specifically represented as finite element models (FEMs), are extensively employed in modeling tissue deformation [15] and are key to solving the 3D-3D non-rigid registration problem [4], [5], [16]. The biomechanical model not only constrains displacements to enforce realistic deformations but also provides insights into volumetric deformation, capturing the complexities of organ deformations beyond surface-level changes.

A. Related work

We focus on registration techniques that utilize a FEM-based biomechanical model to align a preoperative model with an intraoperative point cloud acquired during the surgical procedure. This alignment subsequently aids in determining the locations of subsurface anatomical structures within the intraoperatively deformed liver.

In energy minimization approaches, it is common to integrate a FEM as a strain/deformation energy term to regularize a data term that ensures surface alignment between the preoperative model and the observed intraoperative point cloud data. The strain energy arises within the preoperative model due to the nonrigid displacement field. Rucker *et al.* [4] assumed the posterior side of the organ drove the deformation, then iteratively updated parameters that described the boundary condition and rigid transformation. Based on the similar parameters formation, the framework was further extended to impose constraints from the ligament [9] of the liver and vascular features [1]. The method proposed by Modrzejewski *et al.* [6] includes an iterative closest points (ICP)-based data term, a collision term preventing self-collision, and a strain energy term. Khallaghi *et al.* [17] proposed a framework referred to as the GMM-FEM method in the context of MRI and transrectal ultrasound (TRUS) prostate registration. This method incorporates the FEM into a coherent point drift (CPD) algorithm [18] as the regularization term and uses a Gaussian-mixture model to represent the preoperative surface. The strain energy term can also be minimized without the data term, as shown in the work presented by Peterlik *et al.* [3], where strain energy is minimized while satisfying the geometric constraints searched from ICP.

A limited number of methods directly incorporate the FEM into the data term. Mestdagh *et al.* [16], [19] integrated the FEM into the data term and solved it in an optimal control formulation. However, this approach necessitates manually identifying zero boundary conditions (ZBCs) and force locations.

Instead of incorporating the FEM as a data term or a strain/deformation term, Suwelack *et al.* [5] formulated the movement of the preoperative model to the intraoperative surface as an electrostatic–elastic problem, which the FEM solves. The preoperative model is assumed to be electrically charged and is attracted to the oppositely charged intraoperative surface by its electric potential field.

In deep learning-based techniques, such as neural networks, the biomechanical model is employed to simulate various deformations for training the neural network. Pfeiffer *et al.* [20] proposed V2Snet (volume-to-surface registration network), designed to estimate the deformation of a volume mesh to an intraoperative surface. Tagliabue *et al.* [21] introduced BANet (binary-attachment network) to predict the locations of the attachment points during tissue dissection. The predicted attachment points can be used as ZBCs to update a patient-specific biomechanical model intraoperatively [7].

Although utilizing the FEM as strain energy might restrict deformation, it fails to ensure coherent movement of volumetric vertices to maintain the original geometry. On the

other hand, the direct solution of the FEM-based data term requires identifying Zero-Boundary Conditions (ZBCs) and force locations, as demonstrated in the existing method by Mestdagh *et al.* [16].

Despite the numerous 3D-3D non-rigid registration methods that have been proposed, the liver registration community has limited access to their implementations, with only a few options available [16], [17], [20]. Furthermore, there is a scarcity of publicly available liver registration datasets [5], [6], [22].

B. Contributions

In this paper, we introduce a novel 3D-3D non-rigid registration method that directly incorporates the FEM into the data term. Notably, our approach eliminates the need to manually identify ZBCs and force locations, setting it apart from existing methods. To account for the potential presence of noise associated with the reconstructed intraoperative point clouds, we integrate L2 regularization on the gradient of force magnitudes to ensure spatial smoothness. The optimization process involves an accelerated proximal gradient algorithm and a proposed optimal step decision to enhance acceleration and improve accuracy.

We validate our method using simulated and phantom datasets and two public datasets. Comparative assessments include validation against a learning-based learning-based approach and an optimization-based method utilizing FEM as regularization. The accuracy and robustness of our method relative to the benchmarks demonstrate its effectiveness.

Given the limited availability of public datasets and accessible non-rigid registration methods, we aim to contribute to the field by publicly disseminating our constructed liver dataset and the developed registration algorithm, thereby advancing liver registration benchmarks.

II. PRELIMINARY INFORMATION

Before liver surgery, patient-specific biomechanical finite element models are created using preoperative CT and/or MRI scans. These models are based on the patient’s liver geometry derived from imaging scans, along with the material properties assigned to the tissue.

The preoperative liver geometry is represented by a volumetric tetrahedral mesh model Ω comprising n nodes $\mathbf{x} = \{\mathbf{x}_1, \dots, \mathbf{x}_n | \mathbf{x}_i \in \mathbb{R}^3\} \in \mathbb{R}^{3n}$. The preoperative liver surface is represented by a triangular mesh model $\partial\Omega$ composed of n_s nodes $\mathbf{x}_s \in \mathbb{R}^{3n_s}$, which is a subset of the volumetric mesh nodes.

During surgery, the observed intraoperative surface is represented by a point cloud $\mathbf{y} = \{\mathbf{y}_1, \dots, \mathbf{y}_m | \mathbf{y}_i \in \mathbb{R}^3\} \in \mathbb{R}^{3m}$. The intraoperative surface can be obtained from various sources, such as CBCT, an RGBD depth camera, structure light, stereo laparoscope, or manual swabbing with an optically tracked probe.

The objective is to register a preoperative model with deformed intraoperative surface data to enable the mapping of the sub-surface anatomical structures identified in the preoperative images into the intraoperative scene. A preliminary alignment

of the preoperative model with the intraoperative surface is necessary before the non-rigid step, typically achieved through a rigid transformation. Existing IGLS systems commonly perform this alignment manually [23], [24]; nevertheless, the manual alignment can further improve with a variant of the ICP [25], [26].

A. Biomechanical model

When surface forces \mathbf{f} are applied to the liver boundary, the resulting displacements $\mathbf{u} = \{\mathbf{u}_1, \dots, \mathbf{u}_n | \mathbf{u}_i \in \mathbb{R}^3\} \in \mathbb{R}^{3n}$ are a unique solution of the static equilibrium equation:

$$\mathbf{K}\mathbf{u} = \mathbf{f}, \quad (1)$$

where \mathbf{K} the $3n \times 3n$ stiffness matrix determined by the FEM model of the liver geometry and material properties. In the forward problem, the displacement vector \mathbf{u} throughout the domain Ω can be determined if displacements and/or forces on the boundary $\partial\Omega$ are known. The inverse registration problem solves for the boundary forces that generate a displacement field \mathbf{u}^* that approximates the displacement field \mathbf{u} between the partially observed intraoperative surface and preoperative model.

B. Stiffness Matrix and Boundary Conditions

The liver geometry and material properties are encoded in the stiffness matrix of the finite element model. This matrix characterizes the object's resistance to nodal deformation when subjected to nodal forces. In the case of a linearly elastic biomechanical model, [27], Young's modulus (E), and Poisson's ratio (ν) account for the material's elastic properties.

The stiffness matrix, as formulated, is singular and cannot be inverted. This singularity indicates a scenario where the structure lacks defined boundary conditions or constraints, allowing the structure to undergo rigid motion without internal deformations. In such a state, applied forces can result in indeterminate displacements.

The imposition of boundary conditions, specifying the solution's values on the boundary, constrain rigid-body motions. Consequently, the stiffness matrix becomes invertible, enabling the determination of a unique solution for displacements resulting from applied forces. In the context of assessing liver deformation during surgery, it is crucial to identify the locations featuring ZBC, which typically correspond to the attachment points of the liver. This identification is vital for a meaningful and accurate organ behavior simulation.

III. METHODS

Our method employs a forces-driven approach to deform the source model for optimal alignment with the target point cloud. Fig. 1 provides an overview of our registration method. The objective function comprises a surface matching term and an L2 regularization term. The surface matching term utilizes a correspondence matrix generated by a closest point operator and a FEM. Minimization of the objective function is achieved through an accelerated proximal gradient algorithm. During the force optimization phase, we initially determine

the optimal step for calculating Nesterov's accelerated gradient [28]. Subsequently, the gradient is employed to update forces using a proximal point operator. In each iteration, we first update the correspondence matrix via the closest point operator, then update the force through force optimization; finally, we update the displacements using the FEM. After a set number of iterations, the predicted volumetric deformation enables the preoperative volume model to align with the intraoperative point cloud. In the following section, we will detail each of these steps.

A. Objective function

We perform the registration by determining a surface force vector \mathbf{f} which results in a displacement vector \mathbf{u}_f that minimizes the objective function:

$$\min_{\mathbf{f} \in \mathbf{F}} \Phi(\mathbf{f}) = \beta R(\mathbf{f}) + J(\mathbf{u}_f), \quad (2)$$

where J is a data term that measures the discrepancy between the predicted deformed preoperative surface $\partial\Omega_{\mathbf{u}}$ and the observed intraoperative point cloud data, R is a regularization term that enforces a given property on the forces to prevent overfitting of the data term, β is a weight between the data and regularization term, and \mathbf{F} is the set of force vectors containing prior information about the location of nonzero forces on the liver's surface.

Data Term. The data term is given by

$$J(\mathbf{u}) = \frac{1}{2} \|\mathbf{C}(\mathbf{x} + \mathbf{u}) - \mathbf{y}\|^2, \quad (3)$$

where $\mathbf{C} \in \mathbb{R}^{3m \times 3n}$ is a soft correspondence matrix, $\mathbf{x} \in \mathbb{R}^{3n}$ are spatial location of the preoperative mesh nodes, $\mathbf{u} \in \mathbb{R}^{3n}$ are displacements associated with the nodes, and $\mathbf{y} \in \mathbb{R}^{3m}$ is the intraoperative point cloud. The \mathbf{C} will be detailed in Sec. III-B.

The liver biomechanical model can be incorporated into Eq. 3 by using the relationship between \mathbf{u} and \mathbf{f} given by Eq. 1:

$$J(\mathbf{f}) = \frac{1}{2} \|\mathbf{C}(\mathbf{x} + \mathbf{K}^{-1}\mathbf{f}) - \mathbf{y}\|^2. \quad (4)$$

The resulting data term now becomes a function of the forces applied to the surface of the liver.

Regularization Term. We introduce Tikhonov (L2) regularization to enforce the spatial smoothness of the surface forces:

$$R(\mathbf{f}) = \frac{1}{2} \|\nabla_w \mathbf{f}\|^2 = \frac{1}{2} \sum_{i=1}^{n_s} \sum_{j \in N(i)} (\mathbf{f}_j - \mathbf{f}_i)^2 w_{ij}. \quad (5)$$

where \mathbf{f}_i is the force vector at node i , $N(i)$ represents the j nodes connected to node i , and the weight function $w_{ij} = \frac{1}{d_{ij}^\alpha}$. d_{ij} represents the Euclidean distance between node i and j .

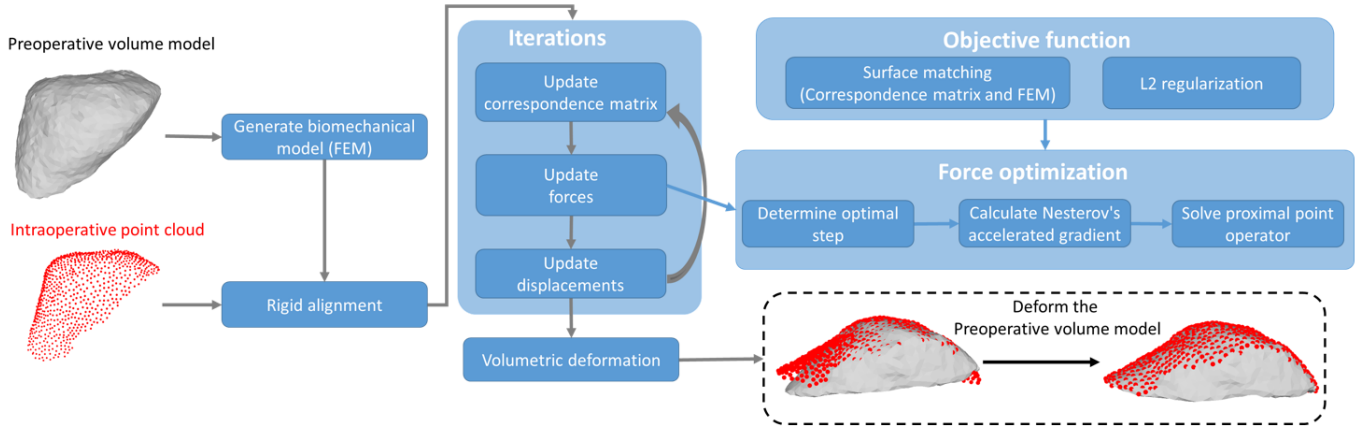


Fig. 1. Overview of the proposed method. The process takes a biomechanical model generated from the preoperative volume model and an intraoperative point cloud. Force optimization leads to volumetric deformation, aligning the preoperative volume model with the intraoperative point cloud.

B. Correspondence Matrix

The correspondence matrix \mathbf{C} contains the correspondences between the points in the intraoperative point cloud and preoperative model. Ideally, if corresponding fiducial points or anatomical landmarks could be consistently identified in pre- and intraoperative spaces, the correspondence matrix would be a one-to-one binary matrix. Obtaining an accurate binary correspondence matrix is nontrivial unless manual annotation is used.

Instead of an accurate binary correspondence matrix, a soft correspondence matrix is often constructed, indicating the probabilistic correspondence between a point in one space and another. The elements C_{ij} of the correspondence matrix \mathbf{C} denote the probability that the intraoperative point \mathbf{y}_i corresponds to the preoperative mesh point $\mathbf{x}_j + \mathbf{u}_j$. Each row of the correspondence matrix should sum to one.

Surface matching methods such as the closest point operator and Gaussian mixture models [17], [18] use the Euclidian distance between points in the pre- and intra-operative space as an alignment metric. Feature-based learning [29] or non-learning [30] methods are used to measure the similarity between features in both spaces and can be used to construct a soft correspondence matrix.

Here we use the closet point operator to construct a soft correspondence matrix. For a given intraoperative point \mathbf{y}_i , the closet point operator determines its closet point $\tilde{\mathbf{y}}_i$:

$$\tilde{\mathbf{y}}_i = \lambda_i(\mathbf{x}_i + \mathbf{u}_i) + \lambda_j(\mathbf{x}_j + \mathbf{u}_j) + \lambda_k(\mathbf{x}_k + \mathbf{u}_k), \quad (6)$$

on the preoperative surface, which is defined by the three nodes $\mathbf{x}_{i,j,k}$, displacements vectors $\mathbf{u}_{i,j,k}$, and barycentric coordinates $\lambda_{i,j,k}$ associated with the surface triangle that contains the closet point.

$\lambda_{i,j,k}$ sums to one, representing confidence values $C_{i,(i,j,k)}$. Thus, the $3m \times 3n$ correspondence matrix is extremely sparse, where each row contains only three non-zero entries corresponding to the barycentric coordinates. The closet point

operator and the resulting correspondence matrix are a function of the undeformed mesh \mathbf{x} , intraoperative point cloud \mathbf{y} , and the nodal displacements \mathbf{u} . The correspondence matrix is recalculated during the iterative registration using the current estimate of the displacements.

C. Optimization

Nesterov's accelerated gradient [28] and a proximal point operator [31] are used to minimize the objective function Eq. 2. The following steps

$$\mathbf{p}^k = \mathbf{f}^k + \frac{k}{k+3}(\mathbf{f}^k - \mathbf{f}^{k-1}), \quad (7)$$

$$\bar{\mathbf{f}}^k = \mathbf{p}^k - \alpha^k \nabla J(\mathbf{p}^k), \quad (8)$$

$$\mathbf{f}^{k+1} = \arg \min_{\mathbf{f}} \left(\frac{\beta}{2} \|\nabla_w \mathbf{f}\|^2 + \frac{1}{2\alpha^k} \|\mathbf{f} - \bar{\mathbf{f}}^k\|^2 \right), \quad (9)$$

are iterated until a stopping condition is met. k represents the number of current iterations.

Nesterov's accelerated gradient is given by Eq. 7 and Eq. 8. \mathbf{p}^k is a momentum term that carries momentum from the previous iteration. Eq. 8 updates the forces, where $\nabla J(\mathbf{p}^k)$ is the gradient of the data term (Eq. 4) with respect to \mathbf{p} , and α^k is the step size. The $\nabla J(\mathbf{p}^k)$ is given by

$$\nabla J(\mathbf{p}^k) = \left((\mathbf{x} + \mathbf{K}^{-1}\mathbf{p}^k)^T \frac{\partial \mathbf{C}^T}{\partial \mathbf{f}} + \mathbf{K}^{-1}\mathbf{C}^T \right) \cdot \left(\mathbf{C}(\mathbf{x} + \mathbf{K}^{-1}\mathbf{p}^k) - \mathbf{y} \right), \quad (10)$$

where $\frac{\partial \mathbf{C}^T}{\partial \mathbf{f}}$ is a 3-dimensional array (3 tensors). It yields a $3n \times 3m$ matrix when multiplied by the vector $(\mathbf{x} + \mathbf{K}^{-1}\mathbf{p}^k)^T$

Optimal step size estimation. In Nesterov's accelerated gradient, the step is usually fixed. To further accelerate the optimization, we determine the optimal step size α^k by substituting the gradient descent term (Eq. 8) into the data term (Eq. 4) and minimizing it with respect to α :

$$\alpha^k = \arg \min_{\alpha} \frac{1}{2} \left\| \mathbf{C} \left(\mathbf{x} + \mathbf{K}^{-1} (\mathbf{p}^k - \alpha \nabla J(\mathbf{p}^k)) \right) - \mathbf{y} \right\|^2, \quad (11)$$

Setting the derivative of Eq. 11 for α to zero, we can obtain the optimal step size

$$\alpha^k = \frac{\left(\mathbf{C} \mathbf{K}^{-1} \nabla J(\mathbf{p}^k) \right)^T \left(\mathbf{C} (\mathbf{x} + \mathbf{K}^{-1} \mathbf{p}^k) - \mathbf{y} \right)}{\left(\mathbf{C} \mathbf{K}^{-1} \nabla J(\mathbf{p}^k) \right)^T \left(\mathbf{C} \mathbf{K}^{-1} \nabla J(\mathbf{p}^k) \right)}. \quad (12)$$

Proximal point operator, given by the Eq. 9, enforces the force vector \mathbf{f}^{k+1} to be smooth, which is the result of the trade-off between minimizing the function $\|\nabla_w \mathbf{f}\|^2$ and its proximity to $\bar{\mathbf{f}}^{k+1}$.

To solve the proximal equation Eq. 9, an approximate solution is obtained by employing an iterative procedure. The minimization of proximal equation Eq. 9 yields the following equation:

$$\left(\mathbf{I} + \beta \alpha^k \Delta_w \right) \mathbf{f}^{k+1} = \bar{\mathbf{f}}^k, \quad (13)$$

where the graph Laplacian $\Delta_w \mathbf{f}_i$ is given by

$$\Delta_w \mathbf{f}_i = \sum_{j \in N(i)} (\mathbf{f}_i - \mathbf{f}_j) w_{ij}, \quad (14)$$

The approximate solution of the previous equation is obtained by employing a Gauss–Seidel iterative procedure [32] that iteratively updates the unknown component of \mathbf{f}_i^{k+1} , then subsequently used to update the remaining components. The solution can be written component-wise as:

$$\mathbf{f}_i^{k+1} = \frac{\bar{\mathbf{f}}_i^k + \beta \alpha^k \sum_{j \in N(i)} \mathbf{f}_j w_{ij}}{1 + \beta \alpha^k \sum_{j \in N(i)} w_{ij}}. \quad (15)$$

The \mathbf{C} should also be updated with forces being updated. We employ a lagged method, utilizing the nodal displacements \mathbf{u}^k from the previous iteration, to update the correspondence matrix in each iteration.

D. Modifications for Unknown Zero Boundary Conditions and Force Locations

As mentioned in Section II-B, without boundary conditions, the stiffness matrix \mathbf{K} is ill-conditioned and cannot be inverted to give a unique, stable solution. However, determining ZBCs and applied force locations is challenging during liver surgery.

To address these unknowns, we modify the stiffness matrix to stabilize the model. Inspired by the concept of soft springs used by the commercial simulation software SOLIDWORKS® [33], we stabilize the model by adding a soft spring to each node. This corresponds to adding a small stiffness term to the diagonal terms of the stiffness matrix:

$$\mathbf{K} \rightarrow \mathbf{K} + k_{ss} \mathbf{I}, \quad (16)$$

where k_{ss} is the stiffness of the soft spring and \mathbf{I} is the identity matrix. This is analogous to the damping term added

to the stiffness matrix in the work presented by Peterlik *et al.* [3]. The added small stiffness increases the inertia of the liver model being deformed, preventing rigid motion without internal deformations. This approach enables us to allow the forces to be applied at any spatial location on the liver surface.

As a consequence of these two modifications, we no longer need to quantify the actual physical forces applied to the liver's surface; rather, we empower the optimization algorithm to identify both the spatial distribution and magnitude of applied forces that optimally deform the preoperative model to match the intraoperative point cloud.

This novel formulation is a key contributor to our goal of developing an algorithm that allows us to register the preoperative and intraoperative without prior knowledge. As we shall show, these modifications can produce accurate registration results.

IV. EXPERIMENTAL SET-UP

Datasets. The experiments are conducted on the following datasets:

1) *In silico phantom*: As illustrated in Fig. 2, we simulated the deformation of the *in silico* phantom using a linear elastic model with Young's modulus $E = 1$ and a Poisson ratio $\nu = 0.49$. Forces are applied perpendicular to the x-y plane on a liver mesh model obtained from OpenHELP [34]. The resulting deformed surface is cropped to generate the simulated intraoperative point cloud, consisting of 934 vertices. The volumetric preoperative mesh comprises 4291 vertices and 1919 tetrahedra.

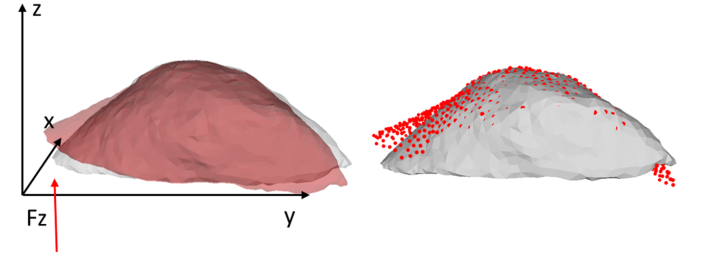


Fig. 2. The generation of an *in silico* phantom. The *in silico* phantom undergoes deformation with forces applied perpendicularly to the x-y plane, visualized by the deformed model in red. The cropped, deformed partial surface, represented as a red point cloud, constitutes the simulated intraoperative point cloud.

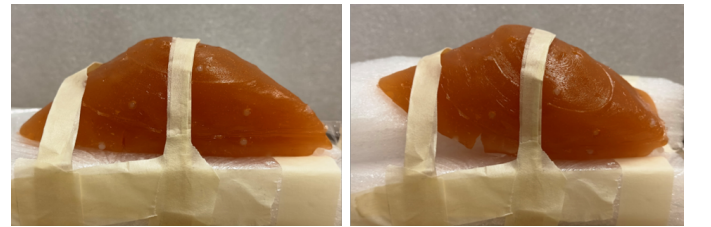


Fig. 3. The generation of a *in vitro* silicone phantom. The undeformed liver phantom is shown on the left, and the deformed one on the right, with wedges added under its posterior surface.

2) *In vitro phantoms*: We created two silicone liver phantoms, A and B, each embedded with 53 and 176 fiducial markers, respectively, fabricated using a 3D-printed mold based on the liver model in OpenHELP [34]. To induce deformation, wedges featuring different gradients were strategically inserted underneath parts of the posterior side of the undeformed phantom, as depicted in Fig. 3 (b). The resulting phantom, with the wedge underneath, is referred to as the deformed phantom. We used the undeformed data as the preoperative data and the deformed data as the intraoperative data. The undeformed liver meshes, featuring around 9000 faces and 4000 vertices, were processed using TetGen [35] to generate the source volumetric meshes consisting of approximately 9000 volumetric vertices and 80000 tetrahedra.

Phantom A and Phantom B underwent three and two deformations respectively, generating five deformed phantoms. We number the deformed phantoms (No.1-3 from phantom A and No.4-5 from phantom B). CT scans were acquired for undeformed and deformed phantoms, and their surfaces and fiducial landmarks were manually segmented. Undeformed and deformed phantoms were manually aligned and refined with an ICP registration implemented by Open3D python library [36]. Initial registration errors are detailed in Table I.

Additionally, partial anterior surfaces were cropped to achieve surface visibility ratios ranging from approximately 18% to 27%, calculated by the ratios of cropped surface areas to the full surface areas, as summarized in Table I.

3) *Open-CAS dataset*: it contains three *in silico* phantoms and one *in vitro* phantom. We refer to [5] for more detail. Deformations of the *in silico* phantoms are created using a non-linear biomechanical model. Regarding the *in vitro* phantom, two intraoperative surfaces from a CT and stereoscopic imaging are included.

4) *Sparse dataset*: We use Set044, Set057, Set067, and Set084 from the Sparse-data non-rigid registration challenge [22], [37], where partial ground truth is available. Intraoperative surfaces are presented with sparse 3D point clouds collected using an optically tracked stylus. We align the sparse data with the undeformed model as we did in the previous Phantoms dataset.

Evaluation. The registration error involves calculating nodal displacement errors for the simulated cases and Target Registration Error (TRE) for the phantom cases. Their calculations share a common form:

$$\text{error}_i = \|\mathbf{Y}_i - \mathbf{W}_i(\mathbf{X}_i)\|_2, \quad (17)$$

where \mathbf{X}_i denotes a fiducial marker location or volumetric vertex position in the undeformed data, \mathbf{Y}_i represents a fiducial marker or vertex position in the deformed data, \mathbf{W}_i signifies the estimated transformation from a registration method for \mathbf{X}_i , and $\|\cdot\|_2$ denotes the Euclidean distance. Considering the four nearest points, the nearest neighbor interpolation is employed to propagate the estimated volumetric deformation to the fiducial markers.

Implementation. The proposed method was implemented in C++ using the Eigen library [38], running on a 3.60 GHZ Intel i9-9900K CPU and 64 GB of RAM.

We use a linear elastic biomechanical liver model for all experiments. Since a linear biomechanical model is employed, Young’s modulus E solely influences the scale of the estimated forces. For this study, we scale the force by setting E to 1. Poisson coefficient is set as $\nu = 0.49$, a typical value for modeling incompressible tissue [39]. Unless otherwise noted, the soft spring constant was set to $k_{ss} = 0.01$, regularization weight to $\beta = 0.05$, and the optimization algorithm was stopped at 200 iterations.

Methods for comparison. We use the official implementations of V2Snet [20] and GMM-FEM [17] as benchmarks for comparison. For V2Snet, we use the official weight included in the implementation. GMM-FEM [17] is an optimization-based method that incorporates the FEM as a strain energy term to regularize the CPD [18]. We implemented it using its suggested parameter values, which were tested in our *in silico* phantom described in Section V-A and gave the lowest errors. Furthermore, we include the Rigid Procrustes that use RANSAC ICP implemented in the Open3D library [36] with ground truth correspondences to estimate the lowest errors that may be achieved via the rigid registration.

V. RESULTS

A. *In silico* Phantom Validation

We initiate our study using a noise-free and fully controlled *in silico* liver phantom to understand how our algorithm performs under various settings.

We first examine the algorithm’s ability to predict ground truth forces when zero boundary conditions and force locations are known. When provided with precise material parameters, exact force locations, and zero boundary conditions (ZBC), our method effectively recovers forces that closely approximate the ground truth forces, as illustrated in Fig. 4 (a). This accurate force recovery translates to minimal registration errors, lower than 2 mm, as depicted in Fig. 4 (b).

Next, we examine a more realistic situation where prior knowledge of the location of zero boundary conditions and forces is unknown. We eliminate ZBCs and set the soft spring constant k_{ss} to 0.05. We explore two scenarios: the former assumes that the forces exist solely on the posterior surface, aligning with the assumption in [4]; the latter assumes that forces can be distributed across the entire surface. As illustrated in Fig. 4 (b), allowing the forces to be applied across the full liver surface yields superior registration results compared to confining the applied forces to the posterior surface. The results also indicate accurate registration results can be obtained without prior knowledge of force locations and ZBCs. As noted before, we are no longer computing the actual physical forces applied to the liver’s surface, but we rather empower the optimization algorithm to determine the fictitious forces that minimize the registration error. Subsequent experiments are conducted, assuming that forces can exist on the full surface.

Furthermore, we show that incorporating Nesterov’s acceleration and updating α enhances the optimization process, resulting in faster convergence and improved accuracy, as depicted in Fig. 4 (c).

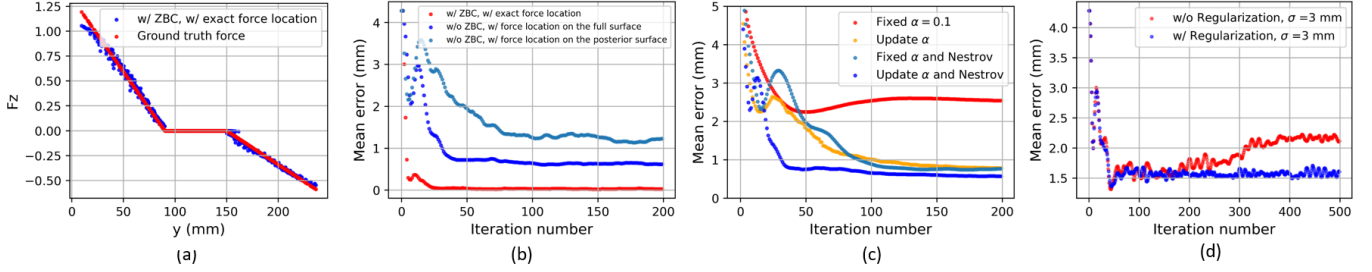


Fig. 4. Results of *in silico* phantom study. (a) Force recovery with correct boundary conditions (ZBCs) and force locations. (b) Examination of priors on registration results. (c) Optimization speed and accuracy through optimization step α update and Nesterov’s acceleration. (d) Effective prevention of overfitting to Gaussian noise ($\sigma = 3$ mm) with L2 regularization.

TABLE I

COMPARISON OF REGISTRATION ERRORS ON THE PHANTOM DATASET, PRESENTED AS MEAN \pm STANDARD DEVIATION (MAX) ERROR IN MILLIMETERS. THE LOWEST MEAN VALUES AND THE LOWEST MAXIMUM VALUES ARE HIGHLIGHTED IN BOLD.

Phantom No.	Visibility ratio	Initial	Rigid Procrustes	V2S-net	GMM-FEM	Proposed Method
1	26.22%	8.31 ± 7.54 (32.76)	3.31 ± 4.24 (20.47)	5.07 ± 4.61 (21.41)	5.17 ± 3.95 (22.58)	1.65 ± 1.48 (7.87)
	100%			3.98 ± 3.87 (18.81)	1.46 ± 2.06 (9.68)	1.02 ± 0.76 (3.50)
2	20.79%	11.50 ± 4.34 (22.43)	5.52 ± 5.27 (23.92)	9.03 ± 5.36 (25.23)	7.58 ± 3.63 (20.10)	1.60 ± 1.17 (6.48)
	100%			5.12 ± 3.44 (17.36)	1.05 ± 1.28 (5.90)	0.96 ± 0.62 (3.69)
3	18.55%	15.82 ± 9.44 (48.13)	9.71 ± 5.77 (24.42)	15.95 ± 6.68 (39.96)	15.97 ± 8.22 (45.70)	4.26 ± 2.99 (15.63)
	100%			14.38 ± 4.93 (31.91)	3.35 ± 3.87 (18.03)	4.55 ± 3.14 (13.26)
4	21.24%	5.36 ± 2.59 (19.21)	2.34 ± 2.76 (17.82)	3.97 ± 2.51 (18.75)	6.62 ± 3.48 (16.56)	0.97 ± 0.64 (3.25)
	100%			3.55 ± 2.26 (15.57)	2.31 ± 2.05 (10.29)	0.46 ± 0.21 (1.17)
5	19.36%	10.73 ± 3.57 (19.16)	1.32 ± 1.49 (9.78)	5.95 ± 2.39 (16.86)	17.54 ± 3.68 (24.10)	0.73 ± 0.66 (5.28)
	100%			2.31 ± 1.19 (9.27)	1.15 ± 1.62 (8.14)	0.36 ± 0.16 (0.98)

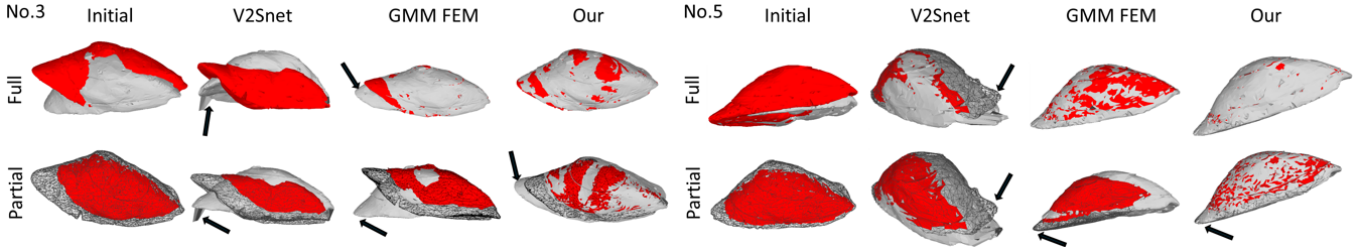


Fig. 5. Qualitative comparison results of registration methods for Phantom datasets No.3 and No.5, presenting both initial undeformed and estimated deformed meshes yielded by all the methods. For cases with partial data, the edges of the complete deformed meshes are also displayed. The intraoperative point cloud is highlighted in red, and obvious disparities between the mesh and intraoperative point cloud are marked with arrows.

In the end, we examine the effect of the regularization term by introducing Gaussian noise with magnitudes $\sigma = 3$ mm. As shown in Fig. 4 (d), the regularization term prevents the source model from fitting the noise as the iterations progress.

The computation depends on the number of FEM nodes and intraoperative point cloud, as our method relies on the FEM model and the close point operator. The average time per iteration for this dataset is 0.11 seconds, which leads to an overall computation time of 22 seconds over the 200 iterations.

B. In vitro Phantom Validation

Table I summarizes the results for the phantom dataset, comparing the whole and partial surface registration errors of our proposed method relative to those achieved by V2S and GMM-FEM. Our method features a mean TREs below 5 mm across all testing samples. Notably, the differences in mean TREs between our predictions for partial and full surfaces are negligible, typically less than 1 mm. In contrast, GMM-FEM tends to exhibit lower errors on full surfaces, as

illustrated by the mean and max TRE on the full surface of No.5, which are 1.15 ± 1.62 (8.14) mm, compared to the partial surface, featuring an error of 17.54 ± 3.68 (24.10) mm. V2Snet encounters challenges in accurately predicting results for No.3, resulting in a mean TRE exceeding 14 mm and a max TRE larger than 30 mm.

Fig. 5 illustrates several qualitative results that provide the reader with a deeper and more tangible interpretation of the registration performance achieved by our proposed and comparative methods. Notably, blade-like structures are evident in the deformed meshes generated by V2Snet, as indicated by arrows in both No. 3 and No. 5. Specifically, for both the full and partial surface cases of the No.3 phantom, the estimated deformed mesh of V2Snet exhibits discrepancies in fully aligning with the ridge of the target surface. This misalignment is also noticeable in the estimation by GMM-FEM, particularly in the case of the partial surface for the No.3 phantom. In contrast, our method consistently produces reasonable deformations for the full and partial cases of the

No.3 phantom. It’s crucial to note that in the partial surface case of No.3, the predicted left inferior ridge from all methods does not precisely match the inferior ridge of the full target surface. This discrepancy results from the inherent ambiguity associated with partially deformed surfaces, a phenomenon also observed in the partial surface of No.5.

C. Open-CAS dataset

The results are summarized in Table II. In the simulation dataset, featuring over 50% visibility, both GMM-FEM and our method exhibit comparable performance, with differences in mean TRE of less than 1 mm. Notably, for Simulation 2, our method achieves a maximum TRE of around 6 mm, significantly lower than the 10 mm achieved by GMM-FEM. V2Snet struggles to generalize on Simulation 1 and demonstrates a maximum TRE exceeding 20 mm for Simulations 2 and 3. The partial CT and stereo-reconstructed surfaces present approximately 20% partial visibility, posing a challenge. In this scenario, our method outperforms all others, yielding the lowest mean and max TRE.

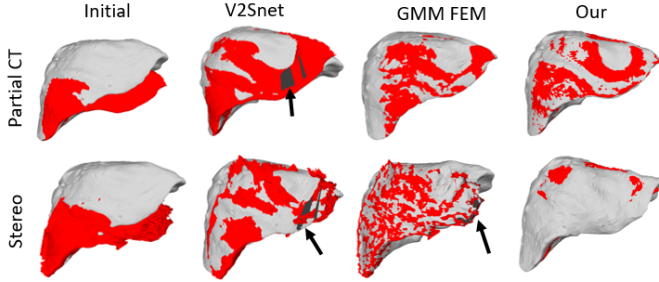


Fig. 6. Qualitative results achieved using the *in silico* phantom cases of the Open-CAS dataset, showing both the initial and estimated meshes. The intraoperative point cloud is highlighted in red, and obvious disparities between the registered preoperative mesh and intraoperative point cloud are marked with arrows.

The qualitative results in Fig. 6 support these findings. As observed previously, V2Snet generates deformed meshes featured with blade-like faces, evident in both cases in Fig. 6. GMM-FEM exhibits a similar phenomenon for the deformed mesh on the stereo-reconstructed surface. In contrast, our method consistently produces deformed meshes that maintain a realistic shape.

D. Sparse dataset

The registration errors are detailed in Table III. Notably, V2Snet was excluded from this particular test as it necessitates intraoperative data in the form of meshes. Our method demonstrates consistent performance, with a mean TRE below 5 mm and a max TRE across all testing samples of less than 7 mm. In contrast, GMM-FEM exhibits a mean TRE exceeding 5 mm on Set044 and Set067, with a max TRE surpassing 7 mm in all samples.

Qualitative results for Set044 in Fig. 7 reveal challenges for GMM-FEM in aligning the left and right inferior ridges of the liver, a task where our method excels in accurately fitting the intraoperative point cloud.

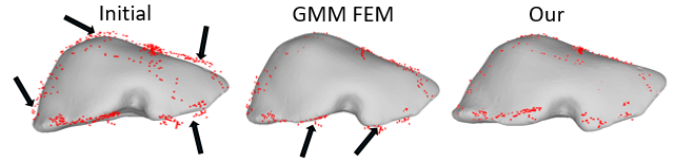


Fig. 7. Qualitative results for Set044 in the Sparse dataset, presenting the initial and estimated deformed meshes. The intraoperative point cloud is highlighted in red, and obvious disparities between the mesh and intraoperative point cloud are marked with arrows.

E. Parameter Sensitivity Analysis

The proposed method relies on three parameters: (1) k_{ss} , a stabilizing parameter for the solution; (2) β , a parameter regulating the spatial smoothness of the estimated forces; and (3) Poisson’s ratio ν , defining the compressibility of the tissue. To understand the sensitivity of our method to the parameters, we vary each parameter individually while keeping the others constant. We examine their impact on registration errors using the *in silico* phantom and the partial case of No.1 phantom in Sec. V-B.

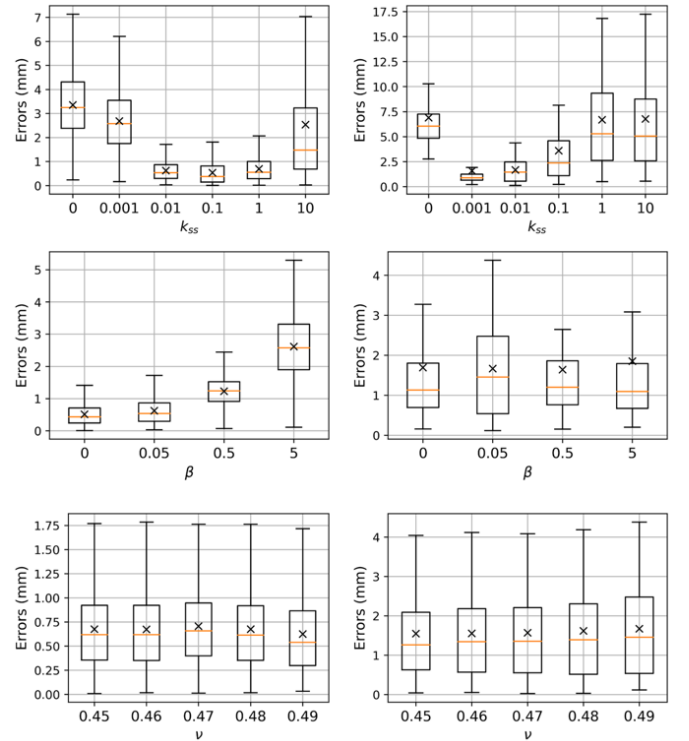


Fig. 8. Parameter sensitivity analysis for k_{ss} , β , and ν performed on the *in silico* phantom (first column) and the partial case of Phantom No. 1 (second column). The median and mean values are represented by orange lines and crosses, respectively.

As illustrated in Fig. 8, the registration outcomes exhibit a degree of sensitivity to the parameter k_{ss} . The default setting of $k_{ss} = 0.01$ shows competitive performance, outperforming other values on the *in silico* phantom. However, the other value $k_{ss} = 0.001$ yields the minimum errors on the phantom data. In previous sections, we found that $k_{ss} = 0.01$ provides reasonable errors across all testing samples. Hence, while

TABLE II

COMPARISON OF REGISTRATION ERRORS ON THE OPEN-CAS DATASET. MEAN \pm STANDARD DEVIATION (MAX) ERROR IN MILLIMETERS IS PRESENTED. THE LOWEST MEAN VALUES AND THE LOWEST MAXIMUM VALUES ARE HIGHLIGHTED IN BOLD.

	Visibility	Initial	Rigid Procrustes	V2S-net	GMM-FEM	Proposed Method
Simulation 1	55.60%	9.97 \pm 8.28 (35.03)	5.88 \pm 6.82 (25.36)	10.92 \pm 9.29 (38.31)	1.90 \pm 1.21 (9.21)	1.65 \pm 1.17 (9.95)
Simulation 2	58.68%	7.47 \pm 7.56 (29.22)	6.45 \pm 26.13 (7.61)	3.06 \pm 3.25 (29.22)	1.98 \pm 1.36, (9.87)	1.42 \pm 1.10 (5.95)
Simulation 3	63.46%	9.17 \pm 11.79 (56.68)	9.16 \pm 13.62 (57.77)	4.91 \pm 5.87 (56.68)	1.80 \pm 1.09 (7.23)	1.77 \pm 1.38 (7.56)
Phantom (partial CT)	19.01%	23.86 \pm 15.07 (46.59)	13.95 \pm 9.34 (25.95)	6.82 \pm 3.40 (11.50)	6.80 \pm 3.61 (12.40)	4.28 \pm 1.56 (6.75)
Phantom (Stereo)	\sim 20%			12.88 \pm 2.90 (16.68)	15.16 \pm 3.59 (21.56)	11.92 \pm 1.50 (14.82)

TABLE III

COMPARISON OF REGISTRATION ERRORS ON THE SPARSE DATASET. MEAN \pm STANDARD DEVIATION (MAX) ERROR IN MILLIMETERS IS PRESENTED. THE LOWEST MEAN VALUES AND THE LOWEST MAXIMUM VALUES ARE HIGHLIGHTED IN BOLD.

Set	Initial	Rigid Procrustes	GMM-FEM	Proposed Method
044	11.15 \pm 4.73 (24.10)	6.42 \pm 5.11 (18.89)	5.69 \pm 3.48 (16.68)	3.67 \pm 1.24 (6.32)
057	14.25 \pm 2.01 (19.39)	6.50 \pm 5.34 (19.69)	4.43 \pm 2.28 (10.33)	3.14 \pm 1.34 (5.83)
067	8.08 \pm 2.13 (13.58)	3.10 \pm 2.35 (9.75)	6.35 \pm 2.08 (10.28)	2.66 \pm 1.41 (5.48)
084	14.74 \pm 2.01 (19.39)	3.31 \pm 2.57 (10.97)	4.43 \pm 1.47 (7.29)	2.43 \pm 1.11 (4.45)

refining this parameter could potentially enhance results, k_{ss} values between 0.01 and 0.1 consistently yield satisfactory outcomes. To be noted, when $k_{ss} = 0$ (no added soft spring stiffness), the registration errors are all obviously larger than the errors when we set k_{ss} values between 0.01 and 0.1.

For the *in silico* phantom without added noise, increasing β leads to escalating errors. However, for dealing with phantoms that include noise, such as segmentation noise in CT scans, varying β results in stable performance.

The default setting of Poisson’s ratio $\nu = 0.49$ corresponds to nearly incompressible tissue behavior. While some prior studies [1], [4] adopt $\nu = 0.45$, our experiments involving variations from 0.45 to 0.49 show stable performance on both the *in silico* and *in vitro* phantoms.

VI. DISCUSSION

We have presented a novel non-rigid 3D-3D registration method that incorporates FEM within the data term and eliminates the need to identify zero boundary conditions and force locations.

To eliminate the need for priors, we first introduce a soft spring modification to the stiffness matrix. This modification has been demonstrated to substantially reduce registration errors, as evidenced in the first row of Fig 8. Secondly, the method is designed to search for optimal forces autonomously. In the absence of manually identified ZBC and force locations, this strategy is more beneficial than the previous approaches [4] of constraining force locations to predefined areas, such as the posterior surface, shown in Fig. 4 (b). Furthermore, our method incorporates L2 regularization that imposes spatial smoothness. The L2 regularization ensures the model remains robust under conditions where the intraoperative point cloud is noisy, as shown in Fig. 4 (d). In addition, our proposed optimal step determination, as demonstrated in Fig. 4 (c), eliminates the need for manual tuning of the step size parameter and leads to quicker convergence and lower error.

We have evaluated our method across various datasets, encompassing our phantom datasets, the Open-CAS dataset, and the Sparse dataset. Moreover, in direct comparisons with two

alternative methods, V2Snet and GMM-FEM, our approach consistently outperforms or shows comparable performance, as elaborated in Sections V-B, V-C, and V-D.

While GMM-FEM incorporates FEM into the strain energy, regularizing the deformation field estimated by the CPD registration method, it does not guarantee faithful preservation of the original geometry (i.e., vertex connectivity) of the deformed surface. This becomes apparent in situations with noisy intraoperative point cloud data, as illustrated in Fig. 6. In contrast, our approach, where FEM inherently guides the deformation, ensures the maintenance of volumetric vertex connectivity, preserving the geometry during deformation. Furthermore, as demonstrated in Section V-B, GMM-FEM exhibits sensitivity to the visibility of the intraoperative surface, as highlighted in its original paper [17].

V2Snet utilizes FEM to construct a training dataset [20]. While it shows competitive results in specific instances, its overall performance and generalization capabilities require improvement. Nevertheless, the use of learning-based methods, offering prior information, has the potential to assist optimization methods in achieving faster and more accurate results.

To be noted, before performing the non-rigid registration, it is crucial to (1) perform a optimal rigid alignment, (2) minimize the intraoperative liver surface reconstruction errors, and (3) ensure a high quality surface characterized by sufficient convergence. These considerations are prerequisites for the problem. Otherwise, our method, like any other, may result in inaccurate registration. However, such registration inaccuracies may be mitigated, provided other constraints besides the intraoperative surface are available, such as vascular features and ligaments from ultrasound [1].

VII. CONCLUSION

We have presented a novel non-rigid 3D-3D registration method that seamlessly integrates a biomechanical model into the surface-matching term without relying on priors. By embedding the biomechanical model in the surface-matching term, the estimated deformation is forced to preserve the geometry of the preoperative model. Experiments on our *in silico* phantom and *in vitro* phantom datasets and two public datasets demonstrate the method’s efficacy in achieving accurate registration results and preserving original geometry. Furthermore, our constructed phantom dataset and method move the benchmarking liver registration, a valuable addition considering the limited availability of open-source datasets and methods. In future work, we plan to implement the algorithm on GPUs, research the integration of learning-based approaches.

REFERENCES

- [1] J. S. Heiselman, W. R. Jarnagin, and M. I. Miga, "Intraoperative correction of liver deformation using sparse surface and vascular features via linearized iterative boundary reconstruction," *IEEE transactions on medical imaging*, vol. 39, no. 6, pp. 2223–2234, 2020.
- [2] J. N. Smit, K. F. Kuhlmann, B. R. Thomson, N. F. Kok, T. J. Ruers, and M. Fusaglia, "Ultrasound guidance in navigated liver surgery: toward deep-learning enhanced compensation of deformation and organ motion," *International journal of computer assisted radiology and surgery*, pp. 1–9, 2023.
- [3] I. Peterlik, H. Courtecuisse, R. Rohling, P. Abolmaesumi, C. Nguan, S. Cotin, and S. Salcudean, "Fast elastic registration of soft tissues under large deformations," *Medical image analysis*, vol. 45, pp. 24–40, 2018.
- [4] D. C. Rucker, Y. Wu, L. W. Clements, J. E. Ondrake, T. S. Pfeiffer, A. L. Simpson, W. R. Jarnagin, and M. I. Miga, "A mechanics-based nonrigid registration method for liver surgery using sparse intraoperative data," *IEEE transactions on medical imaging*, vol. 33, no. 1, pp. 147–158, 2013.
- [5] S. Suwelack, S. Röhl, S. Bodenstedt, D. Reichard, R. Dillmann, T. dos Santos, L. Maier-Hein, M. Wagner, J. Wünscher, H. Kennigott, *et al.*, "Physics-based shape matching for intraoperative image guidance," *Medical physics*, vol. 41, no. 11, p. 111901, 2014.
- [6] R. Modrzejewski, T. Collins, B. Seeliger, A. Bartoli, A. Hostettler, and J. Marescaux, "An in vivo porcine dataset and evaluation methodology to measure soft-body laparoscopic liver registration accuracy with an extended algorithm that handles collisions," *International journal of computer assisted radiology and surgery*, vol. 14, no. 7, pp. 1237–1245, 2019.
- [7] A. Mendizabal, E. Tagliabue, and D. Dall'Alba, "Intraoperative estimation of liver boundary conditions from multiple partial surfaces," *International Journal of Computer Assisted Radiology and Surgery*, pp. 1–8, 2023.
- [8] Z. Yang, R. A. Simon, and C. A. Linte, "Disparity refinement framework for learning-based stereo matching methods in cross-domain setting for laparoscopic images," *Journal of Medical Imaging*, vol. 10, no. 4, p. 045001, 2023.
- [9] J. S. Heiselman, L. W. Clements, J. A. Collins, J. A. Weis, A. L. Simpson, S. K. Geevarghese, T. P. Kingham, W. R. Jarnagin, and M. I. Miga, "Characterization and correction of intraoperative soft tissue deformation in image-guided laparoscopic liver surgery," *Journal of Medical Imaging*, vol. 5, no. 2, pp. 021203–021203, 2018.
- [10] D. Lee, W. H. Nam, J. Y. Lee, and J. B. Ra, "Non-rigid registration between 3d ultrasound and ct images of the liver based on intensity and gradient information," *Physics in Medicine & Biology*, vol. 56, no. 1, p. 117, 2010.
- [11] M. Labrunie, D. Pizarro, C. Tilmant, and A. Bartoli, "Automatic 3d/2d deformable registration in minimally invasive liver resection using a mesh recovery network," in *Medical Imaging with Deep Learning*, 2023.
- [12] Y. Espinel, L. Calvet, K. Botros, E. Buc, C. Tilmant, and A. Bartoli, "Using multiple images and contours for deformable 3d-2d registration of a preoperative ct in laparoscopic liver surgery," in *International Conference on Medical Image Computing and Computer-Assisted Intervention*, pp. 657–666, Springer, 2021.
- [13] T. Collins, D. Pizarro, S. Gasparini, N. Bourdel, P. Chauvet, M. Canis, L. Calvet, and A. Bartoli, "Augmented reality guided laparoscopic surgery of the uterus," *IEEE Transactions on Medical Imaging*, vol. 40, no. 1, pp. 371–380, 2020.
- [14] B. Deng, Y. Yao, R. M. Dyke, and J. Zhang, "A survey of non-rigid 3d registration," in *Computer Graphics Forum*, vol. 41, pp. 559–589, Wiley Online Library, 2022.
- [15] J. Zhang, Y. Zhong, and C. Gu, "Deformable models for surgical simulation: a survey," *IEEE reviews in biomedical engineering*, vol. 11, pp. 143–164, 2017.
- [16] G. Mestdagh and S. Cotin, "An optimal control problem for elastic registration and force estimation in augmented surgery," in *Medical Image Computing and Computer Assisted Intervention–MICCAI 2022: 25th International Conference, Singapore, September 18–22, 2022, Proceedings, Part VII*, pp. 74–83, Springer, 2022.
- [17] S. Khallaghi, C. A. Sánchez, A. Rasoulian, Y. Sun, F. Imani, A. Khojaste, O. Goksel, C. Romagnoli, H. Abdi, S. Chang, *et al.*, "Biomechanically constrained surface registration: Application to mr-trus fusion for prostate interventions," *IEEE transactions on medical imaging*, vol. 34, no. 11, pp. 2404–2414, 2015.
- [18] A. Myronenko and X. Song, "Point set registration: Coherent point drift," *IEEE transactions on pattern analysis and machine intelligence*, vol. 32, no. 12, pp. 2262–2275, 2010.
- [19] G. Mestdagh, "An optimal control formulation for organ registration in augmented surgery," 2022.
- [20] M. Pfeiffer, C. Riediger, S. Leger, J.-P. Kühn, D. Seppelt, R.-T. Hoffmann, J. Weitz, and S. Speidel, "Non-rigid volume to surface registration using a data-driven biomechanical model," in *International Conference on Medical Image Computing and Computer-Assisted Intervention*, pp. 724–734, Springer, 2020.
- [21] E. Tagliabue, D. Dall'Alba, M. Pfeiffer, M. Piccinelli, R. Marin, U. Castellani, S. Speidel, and P. Fiorini, "Data-driven intra-operative estimation of anatomical attachments for autonomous tissue dissection," *IEEE Robotics and Automation Letters*, vol. 6, no. 2, pp. 1856–1863, 2021.
- [22] E. L. Brewer, L. W. Clements, J. A. Collins, D. J. Doss, J. S. Heiselman, M. I. Miga, C. D. Pavas, and E. H. Wisdom III, "The image-to-physical liver registration sparse data challenge," in *Medical Imaging 2019: Image-Guided Procedures, Robotic Interventions, and Modeling*, vol. 10951, pp. 364–370, SPIE, 2019.
- [23] B. Acidi, M. Ghallab, S. Cotin, E. Vibert, and N. Golse, "Augmented reality in liver surgery, where we stand in 2023," *Journal of Visceral Surgery*, 2023.
- [24] N. Golse, A. Petit, M. Lewin, E. Vibert, and S. Cotin, "Augmented reality during open liver surgery using a markerless non-rigid registration system," *Journal of Gastrointestinal Surgery*, vol. 25, pp. 662–671, 2021.
- [25] P. J. Besl and N. D. McKay, "Method for registration of 3-d shapes," in *Sensor fusion IV: control paradigms and data structures*, vol. 1611, pp. 586–606, Spie, 1992.
- [26] L. W. Clements, W. C. Chapman, B. M. Dawant, R. L. Galloway Jr, and M. I. Miga, "Robust surface registration using salient anatomical features for image-guided liver surgery: algorithm and validation," *Medical physics*, vol. 35, no. 6Part1, pp. 2528–2540, 2008.
- [27] J. Bonet and R. D. Wood, *Nonlinear continuum mechanics for finite element analysis*. Cambridge university press, 1997.
- [28] Y. Nesterov, "A method for unconstrained convex minimization problem with the rate of convergence," 1983.
- [29] Z. Yang, R. Simon, and C. A. Linte, "Learning feature descriptors for pre-and intra-operative point cloud matching for laparoscopic liver registration," *International Journal of Computer Assisted Radiology and Surgery*, pp. 1–8, 2023.
- [30] M. R. Robu, J. Ramalhinho, S. Thompson, K. Gurusamy, B. Davidson, D. Hawkes, D. Stoyanov, and M. J. Clarkson, "Global rigid registration of ct to video in laparoscopic liver surgery," *International Journal of Computer Assisted Radiology and Surgery*, vol. 13, no. 6, pp. 947–956, 2018.
- [31] N. Parikh and S. Boyd, "Proximal algorithms," *Foundations and trends® in Optimization*, vol. 1, no. 3, pp. 127–239, 2014.
- [32] H. Jeffreys and B. Jeffreys, *Methods of mathematical physics*. Cambridge university press, 1999.
- [33] "Use soft spring to stabilize model." https://help.solidworks.com/2021/english/SolidWorks/cworks/c_Use_Soft_Spring_to_Stabilize_Model.htm, 2021.
- [34] H. Kennigott, J. Wünscher, M. Wagner, A. Preukschas, A. Wekerle, P. Neher, S. Suwelack, S. Speidel, F. Nickel, D. Oladokun, *et al.*, "Open-help (heidelberg laparoscopy phantom): development of an open-source surgical evaluation and training tool," *Surgical endoscopy*, vol. 29, pp. 3338–3347, 2015.
- [35] S. Hang, "Tetgen, a delaunay-based quality tetrahedral mesh generator," *ACM Trans. Math. Softw.*, vol. 41, no. 2, p. 11, 2015.
- [36] Q.-Y. Zhou, J. Park, and V. Koltun, "Open3d: A modern library for 3d data processing," *arXiv preprint arXiv:1801.09847*, 2018.
- [37] J. A. Collins, J. A. Weis, J. S. Heiselman, L. W. Clements, A. L. Simpson, W. R. Jarnagin, and M. I. Miga, "Improving registration robustness for image-guided liver surgery in a novel human-to-phantom data framework," *IEEE transactions on medical imaging*, vol. 36, no. 7, pp. 1502–1510, 2017.
- [38] G. Guennebaud, B. Jacob, *et al.*, "Eigen v3." <http://eigen.tuxfamily.org>, 2010.
- [39] J. L. Sparks and R. B. Dupaix, "Constitutive modeling of rate-dependent stress-strain behavior of human liver in blunt impact loading," *Annals of biomedical engineering*, vol. 36, pp. 1883–1892, 2008.